

Three-dimensional Structure of the Corona during WHPI Campaign Rotations CR-2219 and CR-2223

D. G. Lloveras¹, A. M. Vásquez^{1,2}, F. A. Nuevo^{1,3}, R. A. Frazin⁴, W. Manchester IV⁴, N. Sachdeva⁴, B. Van der Holst⁴, P. Lamy⁵, and H. Gilardy⁵

¹Instituto de Astronomía y Física del Espacio, CONICET-UBA, Ciudad de Buenos Aires, Argentina

²Universidad Nacional de Tres de Febrero, Buenos Aires, Argentina

³Universidad de Buenos Aires, Ciclo Básico Común, Ciudad de Buenos Aires, Argentina

⁴Department of Climate and Space Sciences and Engineering, Univ. of Michigan, Ann Arbor, MI, USA

⁵Laboratoire Atmosphères, Milieux et Observations Spatiales, CNRS & UVSQ, Guyancourt, France

Key Points:

- Tomographic analysis of WHPI rotations indicate a corona 20% less dense and 20% hotter compared to rotations of the SC 23/24 solar minimum.
- The model density and temperature agree with EUV tomography results within 20% and overestimates up to 75% the density from WL tomography.
- The wind model slow/fast component is associated with field lines characterized by larger/lower tomographic electron density and temperature.

Corresponding author: Diego G. Lloveras, dllloveras@iafe.uba.ar

This is the author manuscript accepted for publication and has undergone full peer review but has not been through the copyediting, typesetting, pagination and proofreading process, which may lead to differences between this version and the [Version of Record](#). Please cite this article as [doi: 10.1029/2022JA030406](https://doi.org/10.1029/2022JA030406).

This article is protected by copyright. All rights reserved.

Abstract

Differential emission measure tomography (DEMT) and white light (WL) tomography were applied to study the three-dimensional (3D) structure of the global solar corona for two WHPI campaign periods, Carrington rotations 2219 and 2223. With DEMT, SDO/AIA images were used to reconstruct the 3D coronal electron density and temperature in the range of heliocentric distance $1.02 - 1.25 R_{\odot}$. With WL tomography, SoHO/LASCO-C2 images were used to reconstruct the 3D electron density in the range of heliocentric distance $2.5 - 6.0 R_{\odot}$. The two periods were also simulated with the 3D-MHD Alfvén Wave Solar Model (AWSoM), and its results compared in detail with the reconstructions. The DEMT analysis reveals a 20% less dense and 20% hotter corona than for rotations corresponding to the solar cycle 23/24 deep minimum. The electron density and temperature of the AWSoM model agree with DEMT results within 10% and 20%, respectively, while its electron density overestimates results of WL tomography up to 75%. The slow (fast) component of the terminal wind speed of the model is found to be associated with field lines characterized by larger (smaller) values of the tomographic density and temperature at the coronal base. DEMT reconstructions reveal the coronal plasma to be ubiquitously characterized by temperature variability of up to $\approx 45\%$ over spatial scales of order $\sim 10^4$ km. Taking into account this level of fine-structure by global models may be consequential for their predictions on wave propagation in the corona.

1 Introduction

The Whole Heliosphere and Planetary Interactions (WHPI) initiative, is an internationally coordinated observation and modeling effort focused on characterizing the three-dimensional (3D) heliosphere and the Sun-planetary relationship during the solar cycle (SC) 24/25 minimum epoch. The minimum of activity is of special interest because it allows the study and analysis of the solar corona in its simplest state. This global effort is preceded by the Whole Heliosphere Interval (WHI, Bisi et al., 2011) and the Whole Sun Month (WSM, Galvin & Kohl, 1999) campaigns, focused on studying the 2008 and the 1996 minima, respectively.

Towards the WHPI objectives, solar rotational tomography (SRT) is a valuable observational technique, able to provide a quantitative empirical description of the 3D distribution of fundamental plasma parameters of the solar corona at a global scale. The technique was originally developed by Altschuler and Perry (1972) to reconstruct the 3D distribution of the coronal electron density from white light (WL) coronagraph images. Later on, the differential emission measure tomography (DEMT) technique (Frazin et al., 2009) was developed, which applied to extreme ultraviolet (EUV) images allows reconstruction of the 3D distribution of both the electron density and temperature of the solar corona (Vásquez et al., 2009).

In this work, both WL-SRT and DEMT were used to study two specific WHPI campaign targets, the 2019 total solar eclipse Carrington rotation (CR)-2219 (2019, 29 June through 26 July), and the Parker Solar Probe and STEREO-A closest approach CR-2223 (2019, 16 October through 12 November). Both rotations provide snapshots of the evolving coronal structure as the solar activity approached its SC 24/25 minimum in December 2019. A modern implementation of SRT (Frazin & Janzen, 2002) was applied to WL polarization brightness (pB) images provided by the Solar and Heliospheric Observatory (SoHO) Large Angle and Spectrometric COronagraph (LASCO) C2 instrument, to obtain 3D reconstructions of the electron density of the corona in the heliocentric height range $2.5-6.0 R_{\odot}$. Also, DEMT was applied to EUV images provided by the Solar Dynamics Observatory (SDO) Atmospheric Imaging Assembly (AIA) instrument, to obtain 3D reconstructions of the electron density and temperature of the corona in the heliocentric height range $1.02 - 1.25 R_{\odot}$.

67 In order to realistically and self-consistently model the solar corona and the solar
 68 wind, a common approach for global 3D magneto-hydrodynamic (MHD) models is to
 69 include an additional source term in the momentum equations, such as Alfvén waves as
 70 an empirical WKB term (Ofman, 2010). An example of this general type of models is
 71 the Alfvén Wave Solar atmosphere Model (AWSoM), which is used in this work to model
 72 the solar corona. This global wave driven solar model considers the effect of dissipation
 73 of turbulence due to interaction between counter-propagating Alfvén waves (Van Doors-
 74 selaere et al., 2020). AWSoM is a self consistent 3D physics-based MHD model extend-
 75 ing from the transition region to the upper corona and to 1 AU (van der Holst et al., 2010;
 76 Sokolov et al., 2013; van der Holst et al., 2014). The model is subject to continuous val-
 77 idation with observations as it is updated and improved. Sachdeva et al. (2019) compared
 78 the results of the model during a minimum of activity with DEMT and WL-SRT in a
 79 global fashion. The model has also been recently validated with DEMT reconstructions
 80 in different magnetic structures by Lloveras et al. (2020). More recently (Sachdeva et
 81 al., 2021) conducted a validation study during solar maximum activity. In this work, the
 82 two selected WHPI rotations were simulated with steady-state AWSoM runs, whose re-
 83 sults were compared with the tomographic reconstructions.

84 The previous WSM and WHI campaigns have been the subject of DEMT studies
 85 complemented with potential field source surface (PFSS) models of the global coronal
 86 magnetic field (Lloveras et al., 2017; Vásquez et al., 2011). In this work, the DEMT and
 87 WL-SRT results for the WHPI campaigns were traced along the magnetic field lines of
 88 the AWSoM model simulations, allowing to analyse the tomographic results in different
 89 magnetic structures, as well as to validate the model in different coronal regions and ranges
 90 of heliocentric height. Lamy et al. (2019) carried out a validation study of two 3D-MHD
 91 coronal models in a forward fashion, quantitatively comparing pB images from various
 92 coronagraphs against synthetic images calculated from the 3D electron density of the mod-
 93 els. In this work, a similar quantitative validation of the AWSoM model was carried out
 94 by quantitatively comparing actual EUV and pB images with synthetic images computed
 95 from the 3D electron density and temperature of the model. The relationship between
 96 the terminal solar wind speed of the AWSoM model and the DEMT reconstructed elec-
 97 tron density and temperature at the coronal base was also investigated.

98 In Section 2 the relevant aspects of the tomographic techniques and the AWSoM
 99 model are summarized. Section 3 shows, in 3D detail, the results of the tomographic re-
 100 constructions and the model, and their comparison. Section 4 summarizes and discusses
 101 the main conclusions of this analysis.

102 2 Methodology

103 2.1 WL-SRT and DEMT

104 Both WL-SRT and DEMT make use of time series of images of the solar corona
 105 (in wavelengths for which the corona is optically thin) taken from different view angles,
 106 as provided by solar rotation and the telescope’s orbital motion. The time series is taken
 107 over a period of $\approx 1/2$ synodic rotation to observe the full corona. In the case of the
 108 SoHO/LASCO-C2 and SDO/AIA instruments here used, both in nearly circular orbits
 109 of radius ≈ 1 a.u., this period is ≈ 14 days. The time series of data allows to pose a lin-
 110 ear inversion problem to determine the 3D spatial distribution of specific parameters of
 111 the solar corona. The reconstruction is done over the range of heights covered by the tele-
 112 scope’s field-of-view (FoV) where there is adequate signal strength.

113 The SRT technique applied in this work, for both WL-SRT and DEMT, assumes
 114 a static coronal structure. As a result, tomographic reconstructions are affected by dynamics-
 115 induced artifacts known as “zero density artifacts” (Frazin & Janzen, 2002; Frazin et al.,
 116 2009). ZDAs are non-reconstructed regions in the corona, and affect a relatively small

117 coronal volume in solar minimum conditions such as in the WHPI rotations studied in
 118 this work. Mitigation of dynamics-induced artifacts in 3D tomography has been explored
 119 by Butala et al. (2010) using Kalman-filtering methods (Kalman, 1960). More recently
 120 Vibert et al. (2016) also investigated the use of spatio-temporal regularization of the so-
 121 lution. These methods have both been experimented in the case of WL tomography. Ex-
 122 ploration of the benefits of their application to EUV tomography (used by DEMENT) will
 123 be the focus of future efforts.

124 The coronal volume to be reconstructed is discretized on a spherical grid of N cells,
 125 whose size is set in relation to the resolution and FoV of the images and the cadence of
 126 the time series. The intensity values of each pixel of every image in the time series are
 127 arranged as a very large column vector of M intensity measurements. Each of those in-
 128 tensity values is the result of a line-of-sight (LOS) integral of an unknown coronal quan-
 129 tity times a known weighting factor which depends on the geometry of the observation
 130 and the emission mechanism. Specifically, in the case of WL-SRT the unknown is the
 131 coronal electron density, and in the case of EUV-SRT it is the coronal band's emissiv-
 132 ity. Upon discretization, the LOS integral is transformed into a sum, and the column data
 133 vector of M intensities is equated to a very large $M \times N$ projection matrix (contain-
 134 ing only known terms depending on the observational geometry) multiplied by a column
 135 vector whose N elements are the unknown values of the coronal parameter to be found
 136 in each cell of the computational grid. The non-squared sparse projection matrix is non-
 137 invertible. The inversion is then posed as a multi-dimensional optimization problem with
 138 N unknowns, where the objective function is essentially the squared norm of the differ-
 139 ence between the synthetic and actual data. Upon solving the optimization problem, the
 140 3D distribution of the electron density or the EUV band emissivity is found in the case
 141 of WL-SRT and EUV-SRT, respectively.

142 In DEMENT, the 3D EUV emissivity found in each of the telescope's bands is further
 143 used to solve for a local differential emission measure (DEM) problem. The local DEM,
 144 dubbed LDEM, describes the temperature distribution of the local plasma in each cell
 145 of the tomographic grid. The LDEM of each voxel is modeled as a Gaussian function $\text{LDEM}(T) =$
 146 $G(T; [T_0, \sigma_T, a])$, where T_0 is the centroid, σ_T its standard deviation, and a its amplitude.
 147 The parameters of the LDEM in each voxel are found by minimizing the discrepancy be-
 148 tween the three tomographic values of the EUV band emissivity and the synthetic val-
 149 ues computed from the LDEM (Vásquez et al., 2010). Once the LDEM is determined
 150 in a given voxel, its mean-squared electron density N_e^2 , mean electron temperature T_e ,
 151 and temperature spread W_T , are found by computing its zeroth through second moments,

$$N_e^2 = \int \text{LDEM}(T) dT, \quad (1)$$

$$T_e = \frac{1}{N_e^2} \int \text{LDEM}(T) T dT, \quad (2)$$

$$W_T^2 = \frac{1}{N_e^2} \int \text{LDEM}(T) (T - T_e)^2 dT. \quad (3)$$

152 In the expressions above, the integrals over temperature are carried out over the
 153 joint temperature sensitivity range $[0.5, 3.0]$ MK of the three bands of AIA used in this
 154 work. DEMENT studies systematically reveal that the coronal plasma is ubiquitously char-
 155 acterized by a significant temperature spread W_T within the volume of each voxel of char-
 156 acteristic linear size $\sim 10^4$ km (as detailed below).

157 For more details on SRT the reader is referred to Frazin and Janzen (2002), Vibert
 158 et al. (2016), and references therein. For further discussion on the DEMENT technique and
 159 the LDEM, the reader is referred to Frazin et al. (2009); Vásquez et al. (2010); Nuevo

160 et al. (2015). We detail next the specific setup used for SRT and DENT in the tomo-
 161 graphic reconstructions carried out in this work.

162 In the case of WL-SRT based on LASCO-C2 data, or C2-SRT hereafter, the to-
 163 mographic problem is solved for the electron density of the corona. The 512^2 pixels LASCO-
 164 C2 images have a radial FoV of $2.5\text{--}6.0 R_{\odot}$, so that the linear pixel size is $d \approx 0.02 R_{\odot}$.
 165 The size of the tomographic grid cell is set to $\Delta r = 0.1 R_{\odot}$ in the radial direction and
 166 $\Delta\theta = \Delta\phi = 3^\circ$ in both the latitudinal (θ) and longitudinal (ϕ) directions. The average
 167 radial cell is located at a height $\langle r \rangle = 4.25 R_{\odot}$, and its angular linear size is then
 168 $\langle \Delta l \rangle = \langle r \rangle \times \Delta\theta \approx 0.2 R_{\odot}$. Taking into account the linear pixel size, the average cell
 169 in the plane-of-the-sky is then threaded by $\Delta r \times \langle \Delta l \rangle / d^2 \approx 50$ LOSs. Every LOS is
 170 numerically treated individually, and then a 16-fold binning is applied, so that the average
 171 cell is threaded by three 16-binned LOSs. As for cadence, for these grid a maximum of 4
 172 images per day is possible, as the apparent rotation of the Sun is about the angular span of
 173 four angular cell sizes. In the case of LASCO-C2 we currently use 1 image per day, which is
 174 the available data. In experiments of C2-SRT carried out with different cadences, 1 image per
 175 day has been found to be optimal, as a larger cadence may introduce too many unreconstructed
 176 cells (ZDAs) due to coronal dynamics, so that 14 images have been used for each of the two
 177 rotations here studied. The pB -images used in this work were obtained from the LASCO-C2
 178 Legacy Archive (<http://idoc-lasco-c2-archive.ias.u-psud.fr>),
 179 which provides images with the best-to-date calibration of the instrument (Lamy et al., 2020).
 180

181 In the case of DENT, EUV-SRT is applied to the 171, 193 and 211 Å bands of the
 182 AIA telescope (see Lloveras et al., 2020, for details), and the tomographic problem is solved
 183 for the each band emissivity of the corona. The 4096^2 pixels AIA images are first binned
 184 down to 1024^2 pixels, and have a radial FoV of $1.0\text{--}1.3 R_{\odot}$, so that the linear pixel size
 185 is $d \approx 0.0025 R_{\odot}$. The size of the tomographic grid cell is set to $\Delta r = 0.01 R_{\odot}$ in the
 186 radial direction and $\Delta\theta = \Delta\phi = 2^\circ$ in both the latitudinal (θ) and longitudinal (ϕ)
 187 directions. The average radial cell is located at a height $\langle r \rangle = 1.15 R_{\odot}$, and its angular
 188 linear size is then $\langle \Delta l \rangle \approx 0.04 R_{\odot}$. Taking into account the linear pixel size, the average
 189 cell in the plane-of-the-sky is then threaded by ≈ 64 LOSs. Every LOS is numerically
 190 treated individually, and then a 16-fold binning is applied, so that the average cell
 191 is threaded by four 16-binned LOSs. In the case of EUV-SRT a standard cadence of 4
 192 images per day is used, so that 55 images have been used for each of the two rotations
 193 here studied. The AIA images used in this work were prepared using the up-to-date pro-
 194 cessing and calibration tools provided through the SolarSoftware package.

195 2.2 The AWSoM Model

196 AWSoM is a self-consistent 3D MHD model of the solar corona and inner heliosphere
 197 that addresses the heating of the solar corona by including low-frequency Alfvén wave
 198 turbulence, with proton temperature anisotropy, heat conduction, and radiative cooling
 199 to describe the solar wind. The extended MHD equations, which form the basis of the
 200 AWSoM model are described in detail in Sokolov et al. (2013) and van der Holst et al.
 201 (2014), and validation results from an updated model can be found in Sachdeva et al.
 202 (2019) and Sachdeva et al. (2021). The MHD equations within AWSoM are solved us-
 203 ing the Block-Adaptive-Tree-Solarwind-Roe-Upwind-Scheme (BATS-R-US, Powell et al.,
 204 1999). To simulate the Sun-Earth system, AWSoM comprises both the solar corona and
 205 the inner heliosphere components of the Space Weather Modeling Framework (SWMF)
 206 described in Tóth et al. (2012).

207 AWSoM is driven by the synoptic or synchronic maps derived from the observed
 208 photospheric magnetic, which are used to specify the radial magnetic field at the inner
 209 boundary of the model. Within the model, a Potential Field Source Surface Model (PF-
 210 SSM) is used to extrapolate the 3D magnetic field from the observed photospheric field.

211 The PFSSM may be specified using spherical harmonics or by numerical solution for the
 212 potential field. All three components of the magnetic field specify the initial conditions.
 213 The radial component specifies the boundary condition and is fixed according to the PF-
 214 SSM solution while the longitudinal and latitudinal components of the magnetic field ad-
 215 just freely according to the inner dynamics. The Alfvén wave energy density at the in-
 216 ner boundary is modeled with its Poynting flux scaling with the magnetic field. In the
 217 corona, the model considers wave reflection due to variation of the Alfvén speed along
 218 the propagation direction. Wave energy is specified propagating away from the bound-
 219 ary, while wave energy that impacts the boundary is absorbed. Finally, density and tem-
 220 perature are specified to be uniform.

221 These boundary conditions present limitations to accuracy of the model in two sig-
 222 nificant ways. Any synoptic map suffers from poor visibility at the solar poles. To com-
 223 pensate for this limitation, we use the synoptic magnetograms provided by application
 224 of the Air Force Data Assimilation Photospheric Flux Transport (ADAPT, Arge et al.,
 225 2013) model to synoptic maps of the Global Oscillation Network Group. These ADAPT-
 226 GONG maps provide a physics-based description of the unobserved polar magnetic fields
 227 by incorporating supergranulation, meridional circulation, and differential rotation. Like
 228 any solar coronal model, uncertainties in the observational data used to drive the model
 229 may propagate into the solution space as well. Limitations associated with the obser-
 230 vations of photospheric magnetic field therefore may affect the AWSoM model output.
 231 The ADAPT model produces an ensemble of magnetic field maps that include uncer-
 232 tainty related to different model parameters. The ensemble modelling of the solar wind
 233 solutions can provide a set of solutions that can be compared to observations to find the
 234 best solution (see Sachdeva et al., 2019).

235 The proportionality constant between the Poynting flux of the outward propagat-
 236 ing wave and the local magnetic field at the inner boundary is a free parameter of the
 237 model. During periods of increased magnetic activity, to reduce the excess energy de-
 238 posited in the corona this factor is reduced as compared to its value of $10^6 \text{ W m}^{-2} \text{ T}^{-1}$
 239 during solar minimum (Sachdeva et al., 2021). The Alfvén wave correlation length and
 240 the stochastic heating amplitude and exponent can also be adjusted to match the ob-
 241 servations. For computational purposes, AWSoM makes use of an extended transition
 242 region, so that coronal conditions are achieved at heliocentric distance $r \approx 1.05 R_{\odot}$. At
 243 the inner boundary, the initial electron and proton temperatures (both parallel and per-
 244 pendicular) are set to 50,000 K. The proton number density is overestimated and set to
 245 $5 \times 10^{18} \text{ m}^{-3}$ for the model to be able to replenish the plasma that depletes due to chro-
 246 mospheric evaporation. This leads to an extending transition region as the AWSoM so-
 247 lution relaxes to equilibrium conditions slightly above the inner boundary.

248 Relevant to the analysis of this work is the model’s 3D distribution of the electron
 249 density and temperature, the magnetic field, and the radial component of the solar wind
 250 velocity. A limitation of the density specification described above is that comparisons
 251 against tomographic reconstructions are possible only above $r = 1.05 R_{\odot}$. In its con-
 252 tinuous development, the AWSoM model is the subject of validation efforts with obser-
 253 vations both in the low corona and the heliosphere. In particular, WL-SRT and DENT
 254 have both been used as part of validation studies (Jin et al., 2012; Oran et al., 2015; Sachdeva
 255 et al., 2019, 2021; Lloveras et al., 2017, 2020). The present study constitutes a new con-
 256 tribution in this series of works.

257 2.3 Results along Magnetic Field Lines

258 Once the products of tomographic reconstructions (either C2-SRT or DENT) are
 259 found, and the AWSoM model run has been calculated, the former are traced along the
 260 field lines of the latter, in order to characterize the global thermodynamic state of the

solar corona in distinct magnetic structures. The method, previously applied by (Lloveras et al., 2020), is summarized next.

First, the geometry of sample field lines of the model is determined by numerical integration both inward and outward from starting points set at several heliocentric distances uniformly covering the range $1.02\text{--}1.25 R_{\odot}$ in case of DEMT, and the range $2.5\text{--}6.0 R_{\odot}$ in the case of C2-SRT. At each height one starting point is set every 2° in both latitude and longitude. This distribution of starting points allows to set magnetic field lines that sample the whole volume of the corona in the tomographic computational sphere.

Each traced magnetic field lines is classified as open or closed according to their full geometry. Closed magnetic field line were separated in two segments that extend from the coronal base up to the apex. For each traced open field line and for each segment of the closed field lines, simple functional fits are applied in order to characterize the traced tomographic results in a simple way.

In the case of DEMT, following the previous analysis by Lloveras et al. (2020), a hydrostatic isothermic fit is applied to the electron density as a function of height, and a linear fit is applied to the electron temperature as a function of height, which work well at the height range covered by the DEMT grid ($r \leq 1.25 R_{\odot}$). Specifically, the fits are described by the equations,

$$N_e^{\text{(DEMT)}}(r) = N_0 \exp[-(h/\lambda_N) / (r/R_{\odot})], \quad (4)$$

$$T_e^{\text{(DEMT)}}(r) = T_0 + a h. \quad (5)$$

where in Equation (4), $h \equiv r - 1 R_{\odot}$ is the coronal height measured from the photosphere, $\lambda_N [R_{\odot}]$ is the density scale height, and $N_0 [\text{cm}^{-3}]$ is the electron density of the fit at $h = 0$. In Equation (5), the slope $a [\text{MK}/R_{\odot}]$ is the radial temperature gradient, and $T_0 [\text{MK}]$ is the electron temperature of the fit at $h = 0$.

In the case of C2-SRT, the radial FoV covered by the instrument ($2.5 - 6.0 R_{\odot}$) makes the hydrostatic regime less adequate to fit the electron density as a function of height. Previous works analysing the large-scale coronal structure (Guhathakurta et al., 1996; Kohl et al., 1998; Sittler & Guhathakurta, 1999; Thernisien & Howard, 2006; Lobzin et al., 2008; Cairns et al., 2009; T. Wang et al., 2017; Harding et al., 2019; Morgan, 2019) use a combination of two or more power-law (PL) terms $\propto r^{-p}$, with different exponent values p to describe the observed trends of $N_e(r)$ over a wide range of heights r . In some cases a term r^{-2} is included to describe mass conservation of a constant speed radial outflow at very large values of r , while terms with larger exponents describe the observed trends over smaller values of r . In this work, an optimal goodness-of-fit to the observed $N_e(r)$ over the C2 FoV was found by using a single PL,

$$N_e^{\text{(C2-SRT)}}(r) = N_0 (r/2.5 R_{\odot})^{-p}, \quad (6)$$

where $N_0 [\text{cm}^{-3}]$ is the electron density of the fit at $r = 2.5 R_{\odot}$ (the lowest height of the LASCO-C2 radial FoV), and p is the exponent. The characteristic scale height $\langle \lambda_N \rangle [R_{\odot}]$, height-averaged over the radial FoV, is a physically meaningful quantity that can then be calculated in a straightforward fashion as a function of the PL exponent,

$$\langle \lambda_N \rangle \equiv \left\langle \left| \frac{1}{N_e(r)} \frac{dN_e}{dr}(r) \right|^{-1} \right\rangle = \frac{\langle r \rangle}{p} = \frac{4.25 R_{\odot}}{p}. \quad (7)$$

Once the fits have been applied for each traced field line, the statistical analysis of the results is carried out on the set of field lines that match the following criteria:

- 300 a) The field line must go through at least five tomographic grid cells with reconstructed
 301 data, and there must be at least one data point in each third of the range of heights
 302 spanned by the line. This requirement is set to ensure a reasonably spread sam-
 303 ple of heights along the line.
- 304 b) The confidence level of the fit to the electron density, as well as to the electron
 305 temperature in the case of DENT, must be larger than 90%.
- 306 c) In the case of DENT, the correlation between temperature and heliocentric height
 307 must meet $|\rho(T, r)| > 0.5$, to ensure a linear fit is reasonable.

308 Based on their geometry and thermodynamical properties, the selected magnetic field
 309 lines are then classified in four different types, as indicated below. In the case of DENT,
 310 closed loops are first classified as “small” or “large” depending on their apex being be-
 311 low or above the maximum height of the DENT grid ($1.25 R_{\odot}$), respectively. Also in the
 312 case of DENT, field lines (both closed and open) are further classified as “up” or “down”
 313 upon their fit to $T_e(r)$ increasing or decreasing with heliocentric height r , respectively.
 314 As shown in Section 3.1 below, the magnetically open/closed boundary of the AWSoM
 315 model for the simulated rotations is located always around latitude $\approx 60^\circ$. Taking this
 316 into consideration, in order to separate different coronal structures based on their field
 317 line geometry and their thermodynamics, and similarly to the analysis by Lloveras et al.
 318 (2020), field lines are classified in the four types indicated in Table 1.

319 Section 3 shows in detail the statistical results of DENT, C2-SRT, and AWSoM
 320 for the four classes of field lines here defined.

Table 1. Classification of traced magnetic field lines according to their geometry (open/closed), size (small/large, upon apex being within/outside the range of heights of DENT), their gradient of temperature with height (up/down, see text), and the footpoint latitude θ_0 .

Type Name	Open/Closed	Size	Up/Down	Footpoint Latitude
0	Closed	Small	Down	$ \theta_0 < 50^\circ$
I	Closed	Small	Up	$ \theta_0 < 50^\circ$
II	Closed	Large	Up	$ \theta_0 > 40^\circ$
III	Open	Large	Up	$ \theta_0 > 60^\circ$

321 3 Results

322 3.1 DENT Reconstructions and the AWSoM Model

323 For CRs 2219 and 2223, Figure 1 shows latitude-longitude maps of the electron den-
 324 sity N_e and temperature T_e of both the DENT analysis and the AWSoM model. Maps
 325 are shown at a sample heliocentric height $r = 1.105 R_{\odot}$, in the middle of the range of
 326 heights covered by the DENT computational grid. In the DENT reconstructions, the
 327 larger density and temperature values that characterize the lower latitudes ($|\theta| \lesssim 60^\circ$)
 328 correspond to the equatorial streamer belt, and the lower density and temperature at
 329 larger latitudes correspond to the coronal holes (CHs).

330 For both rotations, there is an overall good consistency between the AWSoM and
 331 DENT maps, both in terms of shape and size of the streamer belt and the CHs, as well
 332 as in the characteristic values and their dynamic range. In the northern hemisphere, the
 333 location and shape of the open/closed (O/C) boundary of the AWSoM model closely matches
 334 the transition of the DENT N_e from larger values in the streamer belt (red/yellow col-

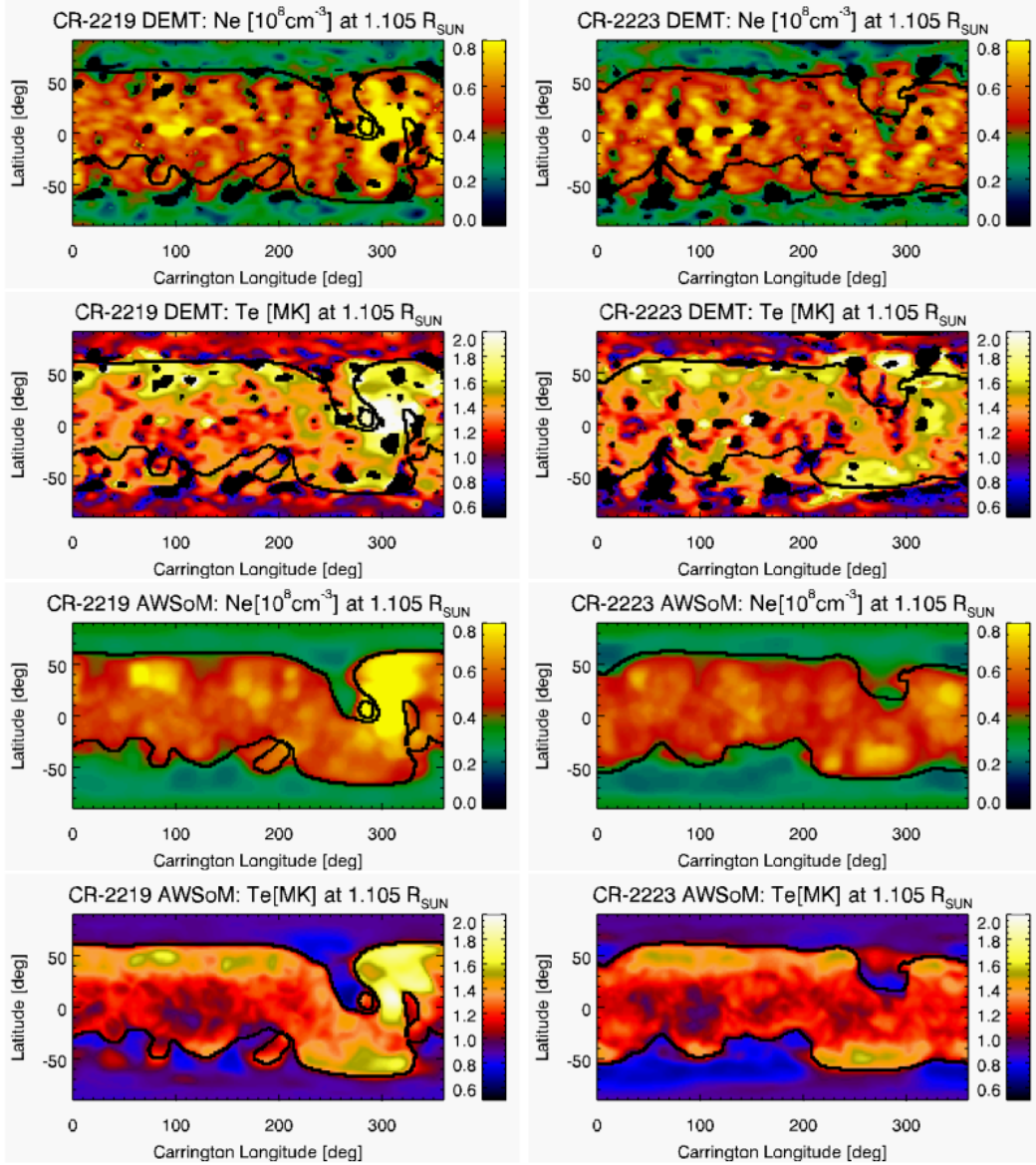


Figure 1. Latitude-longitude maps of electron density N_e and temperature T_e for CR-2219 (left panels) and CR-2223 (right panels) at heliocentric height $1.105 R_{\odot}$ from DEMT (top two panels) and from the AWSoM model (bottom two panels). Black pixels on DEMT maps correspond to non-reconstructed regions. In all maps, the thick-black curves indicate the boundaries between magnetically open and closed regions, based on the AWSoM model.

ors) to smaller CHs values (green/blue colors). The characteristic ratio of electron density between the streamer and the CHs is ≈ 2 . Also across the O/C boundary, the DEMT temperature transitions from larger values within the streamer ($T_e \gtrsim 1.3$ MK) to lower values in the CHs ($T_e \lesssim 1.1$ MK). The characteristic values of both electron density and temperature, detailed in Figures 6-7 below, are consistent with those found in DEMT analysis or rotations selected from the previous two solar minima (Lloveras et al., 2017, 2020). In the southern hemisphere, also for both rotations, the agreement between DEMT

342 results and the AWSoM model is similarly good in the range of Carrington longitudes
 343 $\approx 200\text{--}360^\circ$, but is less satisfactory in the range of Carrington longitudes $\approx 0\text{--}200^\circ$.

344 The value of the mean electron density N_e and temperature T_e in each voxel are
 345 found from the LDEM by means of Eqns. (1)-(2) which, as shown in Figure 1, result in
 346 different characteristic values in the streamer and CH regions. It is interesting to exam-
 347 ine the typical LDEM temperature spread W_T in both regions as well, as determined from
 348 Eqn. (3). The left panel of Figure 2 shows a typical example of LDEM from the streamer
 349 (solid line-style) and from the CHs (dashed line-style). The over-plotted diamonds high-
 350 light the LDEM values at their respective mean electron temperature T_e , while the hori-
 351 zontal lines indicate the temperature spread $T_e \pm W_T$ of each LDEM. While the LDEM
 352 in voxels within the streamer are typically peaked at a temperature $\gtrsim 1.3$ MK, the LDEM
 353 in voxels within the CHs monotonically decrease with increasing temperature, due to the
 354 relatively dominating emissivity of the 171 Å band in that region. Indeed, in voxels of
 355 the CHs the LDEM best predicts the tomographic EUV emissivities by means of a Gaus-
 356 sian model with a negative centroid, as to match the progressively smaller emissivities
 357 of the 171, 193 and 211 Å bands. The Gaussian LDEM model is successful in the whole
 358 DEMT computational volume, predicting the tomographic emissivities to accuracy \lesssim
 359 1% in streamers and $\lesssim 10\%$ in CHs.

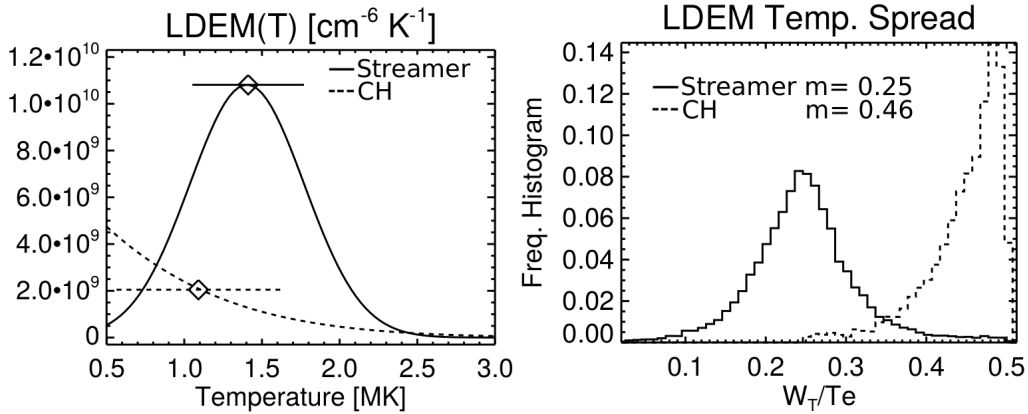


Figure 2. Left panel: characteristic example of LDEM in a tomographic cell corresponding to the streamer (solid line-style) and the CHs (dashed line-style). Over-plotted diamonds highlight the LDEM values at their respective mean electron temperature T_e , while the horizontal lines indicate the temperature spread $T_e \pm W_T$ of each LDEM. Right panel: statistical distribution of the relative temperature spread is W_T/T_e for all the tomographic voxels in both the streamer (solid line-style) and the CHs (dashed line-style).

360 The right panel of Figure 2 shows the statistical distribution of the LDEM temper-
 361 ature spread W_T relative to the LDEM mean temperature T_e , for all the tomographic
 362 voxels in both the streamer (solid line-style) and the CHs (dashed line-style). The ra-
 363 tio W_T/T_e represents the characteristic variability of the electron temperature between
 364 different spatial points within a voxel. The characteristic (median) relative temperature
 365 spread is $W_T/T_e \approx 25\%$ in voxels of the streamer and $\approx 45\%$ in voxels of the CHs. A
 366 similar degree of relative variability is expected to characterize the distribution of elec-
 367 tron density within each voxel, whose scale height along magnetic field lines is propor-
 368 tional to the electron temperature. The plots in Figure 2 correspond to CR-2223, with
 369 results for CR-2219 being virtually the same.

370 Comparison of synthetic images derived from models against actual data is an im-
 371 portant validation test. For all three EUV bands, Figure 3 shows AIA images as well as
 372 synthetic ones, and their comparison. The synthetic EUV images were computed using
 373 the (either DEMA or AWSOM) 3D electron density and temperature, the instrumental
 374 passbands, and the atomic database and plasma emission model CHIANTI V9 (Del Zanna
 375 et al., 2015). The DEMA synthetic images are systematically (and significantly) more
 376 consistent with actual AIA images than the AWSOM synthetic images, as quantified by
 377 the comparative histograms. In these specific images, the East limb longitude corresponds
 378 to Carrington longitude $\approx 155^\circ$, in the center of the region where there is a larger dis-
 379 crepancy between the southern hemisphere O/C boundary of the AWSOM model and
 380 the DEMA density/temperature structure. It is evident that the location of the streamer/CH
 381 boundary of the images (clearly seen in both the 193 and the 211Å bands) is faithfully
 382 reproduced by the DEMA images, while the AWSOM images show this boundary shifted
 383 to lower latitudes in the southern hemisphere. This indicates that the O/C boundary
 384 of the model is not accurate in the southern hemisphere. The location and shape of the
 385 O/C boundary of the model is highly sensitive to the specific synoptic magnetogram used
 386 as boundary condition. This discrepancy is indicating that, for these rotations, the ADAPT-
 387 GONG magnetograms are not able to reproduce the large-scale structure of the CH bound-
 388 ary in this specific region of the southern hemisphere.

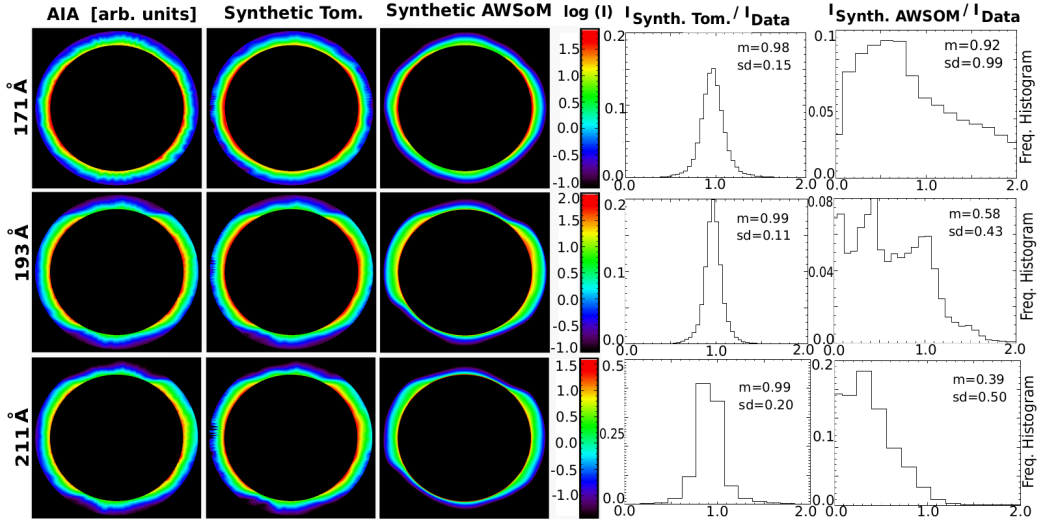


Figure 3. Comparison of actual AIA images (taken on 2019-10-25 UT 03) against synthetic ones, for bands 171, 193 and 211 Å (from top to bottom). The images are masked (black color) outside the FoV radial range $1.02 - 1.25 R_\odot$. From left to right: AIA image, DEMA synthetic image, AWSOM synthetic image, and histograms of the pixel-by-pixel ratio $I_{\text{SYNTH}}/I_{\text{DATA}}$ for DEMA and AWSOM, respectively.

389 For both rotations, DEMA and AWSOM results were traced along the magnetic field
 390 lines given by the MHD model. Figure 4 show the latitude–longitude location (at helio-
 391 centric height $r = 1.105 R_\odot$) of the field lines for which the criteria (a)-(c) of Section
 392 2.3 is met. Using a four-color code, type 0, I, II, and III field lines (see Table 1) are shown
 393 in blue, orange, red, and cyan color, respectively. Figure 4 shows that the streamer belt
 394 is characterized by the presence of magnetic loops of type 0 (down loops), similarly to
 395 previous DEMA studies of solar minima rotations (Nuevo et al., 2013; Lloveras et al.,
 396 2017, 2020). The MHD model is not able of reproducing down loops. In these specific
 397 rotations, the fractional population of down loops is significant but smaller (about half)

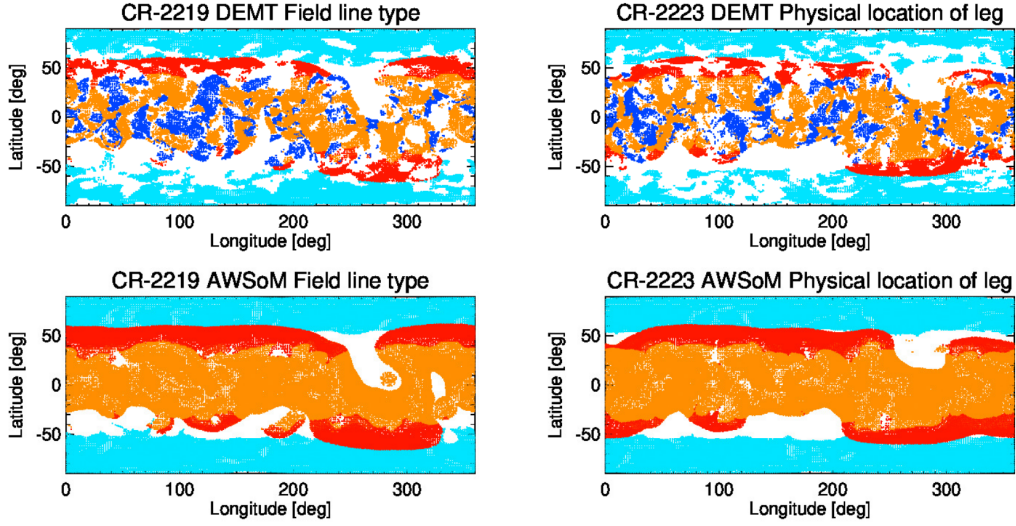


Figure 4. Latitude-longitude position of traced magnetic field lines at heliocentric height $r = 1.105 R_{\odot}$ for CR-2219 (left panels) and CR-2223 (right panels), for which criteria a), b), and c) of Section 2.3 are met. The location of lines of type 0, I, II, and III (see Table 1) is shown in blue, orange, red, and cyan color, respectively.

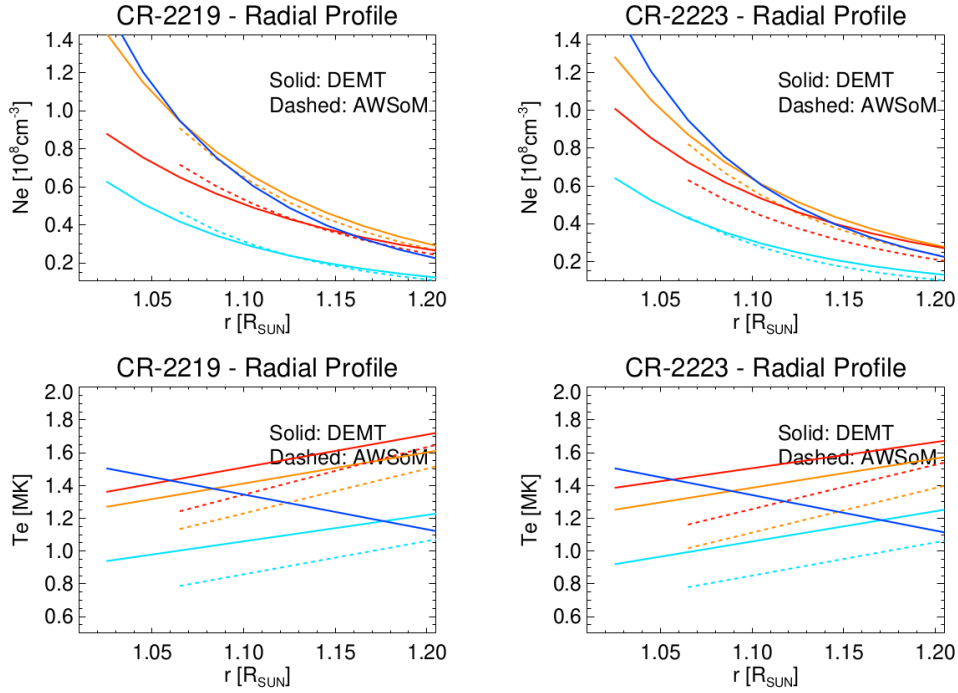


Figure 5. Average fits to $N_e(r)$ (top panels) and $T_e(r)$ (bottom panels) for field lines of type 0 (blue), I (orange), II (red), and III (cyan), for CR-2219 (left panels) and CR-2223 (right panels). Solid lines correspond to DGMT results while dashed lines correspond to the AWSoM model, which does not have type 0 lines.

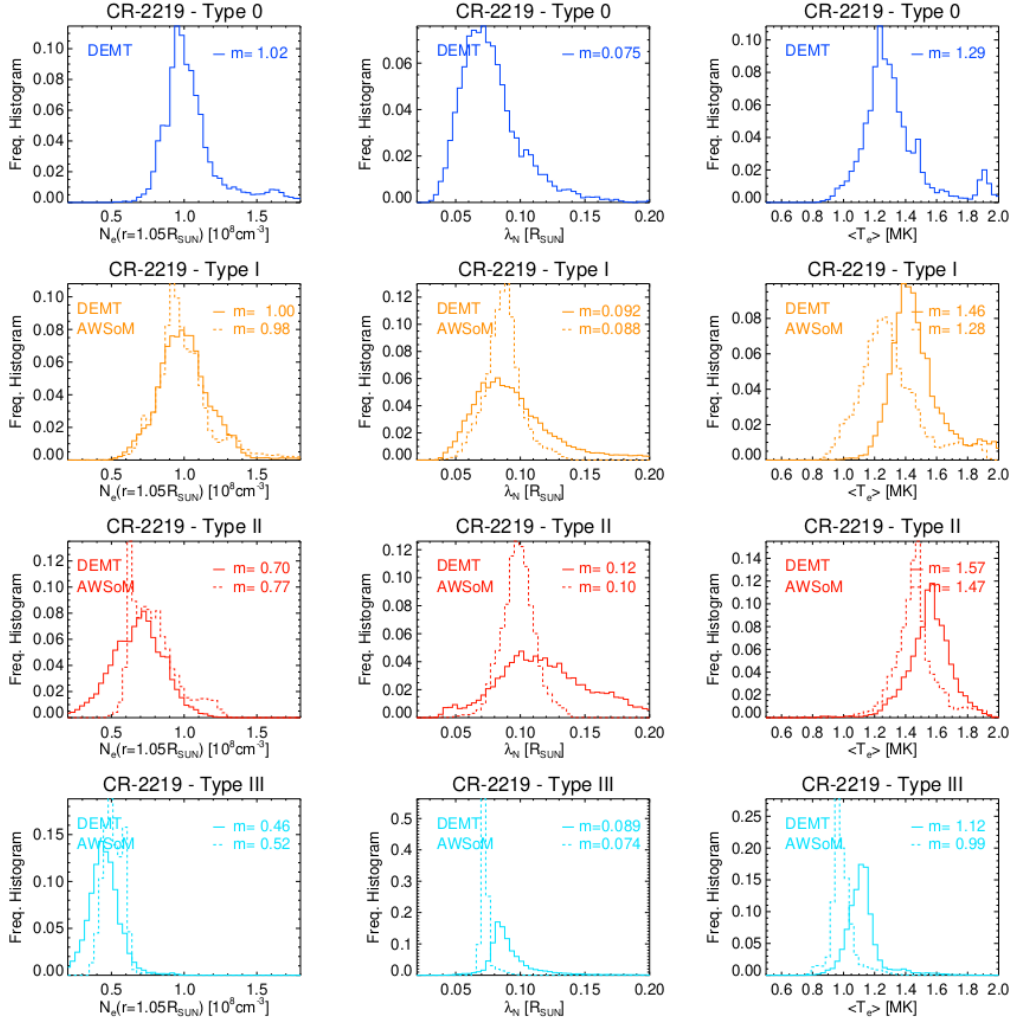


Figure 6. Statistical distribution of the results for CR-2219 from DENT (solid lines) and AWSoM (dashed lines) traced along magnetic field lines of type 0, I, II and III (from top to bottom and using the same color code as in Figure 5). From left to right: electron density at the lowest coronal height of the AWSoM model $N_e(r = 1.055 R_\odot)$, electron density scale height λ_N within the AIA FoV, and field line averaged electron temperature $\langle T_e \rangle$. In each panel the median values m are indicated.

of what was found during rotations of the SC 23/24 deep minimum epoch, as reported by Lloveras et al. (2020).

To provide a summary of the 3D results for both rotations, Figure 5 shows the average fits to $N_e(r)$ and $T_e(r)$, as given by Eqns. (4)-(5), within the AIA FoV for each type of field line defined in Section 2.3, as derived from DENT (solid lines) and the AWSoM model (dashed lines). For both rotations, the electron density results of the AWSoM model are highly consistent with tomographic reconstructions, both in terms of absolute value and scale height. Also for both rotations, the electron temperature of the AWSoM model is very consistent with the tomographic results, both in terms of absolute value and radial gradient, with the model systematically exhibiting temperature values $\approx 15\%$ smaller than the tomographic results.

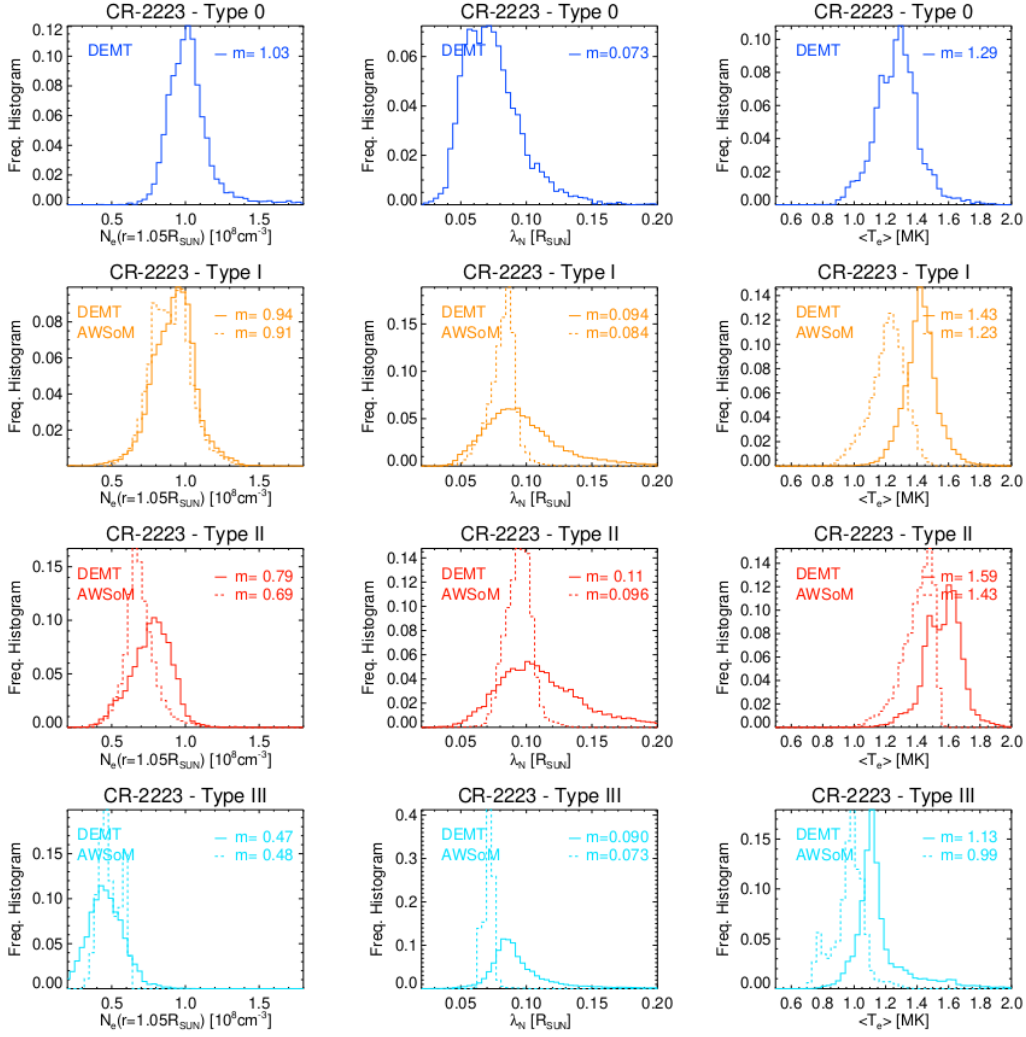


Figure 7. Same as Figure 6 for CR-2223.

409 For the different types of field lines, Figures 6 and 7 show the statistical distribution
 410 of results for CRs 2219 and 2223, respectively. Tomographic results are shown in
 411 solid line style and the AWSoM model results in dashed line style. The left and middle
 412 panels show the electron density at the coronal base (specifically at $r = 1.055 R_{\odot}$, where
 413 the AWSoM model reaches coronal values) and the density scale height. In a similar fash-
 414 ion, the right panels show the field line averaged electron temperature $\langle T_e \rangle$. These plots
 415 reveal in 3D detail the density and temperature structure of both the DEMT reconstruc-
 416 tions and the AWSoM model, being both highly consistent in all regions. From top to
 417 bottom, the left and middle panels of Figs. 6 and 7 show how the electron density at the
 418 coronal base decreases (and the scale height increases) when moving from the core re-
 419 gion of the streamer (type 0 and I field lines) to its outer layers (type II field lines). Also,
 420 the coronal base density and scale height decrease when moving from the streamer out-
 421 to the open region (type III field lines). Similarly, the right panels show how that the
 422 electron temperature increases when moving from the streamer core to its outer layers,
 423 and then decreases when moving out to the open regions. These trends are observed for
 424 both the DEMT results and the AWSoM model.

Table 2. Median value (indicated as “Md”) of the statistical distribution of $N_{\text{CB}} \equiv N_e(r = 1.055 R_{\odot})$, λ_N , and $\langle T_e \rangle$ shown in Figs. 6-7. DENT values are expressed in absolute terms, while AWSoM results are expressed relative to the corresponding DENT value.

Type	Md(N_{CB}) [10^8 cm^{-3}]	Md(λ_N) [R_{\odot}]	Md($\langle T_e \rangle$) [MK]
CR-2219			
0	1.02	0.075	1.29
I	1.00 (- 2%)	0.092 (- 4%)	1.46 (-12%)
II	0.70 (+ 1%)	0.120 (-17%)	1.57 (- 6%)
III	0.46 (+13%)	0.089 (-17%)	1.12 (-12%)
CR-2223			
0	1.03	0.073	1.29
I	0.94 (- 3%)	0.094 (-11%)	1.43 (-14%)
II	0.79 (-13%)	0.110 (-13%)	1.59 (-10%)
III	0.47 (+ 2%)	0.090 (-19%)	1.13 (-12%)

Table 2 summarises a quantitative comparative analysis between the results of the AWSoM model and the DENT reconstructions. Error bars of the DENT products due to their dominating sources of uncertainty (radiometric calibration and tomographic regularization) were determined by Nuevo et al. (2015) and Lloveras et al. (2017). Statistically, the electron density at the coronal base of the AWSoM model matches the reconstructed values within $\approx 1 - 13\%$ accuracy (depending on the specific region and rotation), a difference comparable to the DENT uncertainty level $\Delta N_{\text{CB}} \approx 10\%$. Similarly, the density scale height of the AWSoM model is systematically smaller than the tomographic result within $\approx 4-19\%$ accuracy, differences well beyond the DENT uncertainty level $\Delta \lambda_N \approx 2\%$. Also, the temperature of the AWSoM model is systematically smaller than the tomographic result within $\approx 6-14\%$ accuracy, a difference comparable or larger than the uncertainty in the DENT temperature $\Delta T_e \approx 5\%$.

As a closing remark, it is interesting to quantify the degree of departure of DENT results for electron density and temperature from the values expected for an isothermal hydrostatic plasma. For such a regime, the values of λ_N listed in Table 2 imply electron temperature values that differ from the corresponding listed values of $\langle T_e \rangle$ by 5 to 20%, with the larger departure corresponding the open field region. These differences are relatively small, which is expected at the low heights analyzed by DENT ($r < 1.25 R_{\odot}$), where the wind speed is either negligible (closed region) or rather small (open regions), as analysed in detail by Lloveras et al. (2017).

3.2 C2-SRT Reconstructions and the AWSoM Model

For CRs 2219 and 2223, Figure 8 shows latitude-longitude maps of the electron density N_e of both the C2-SRT analysis and the AWSoM model. Maps are shown at a sample heliocentric height $r = 2.5 R_{\odot}$, the lowest height of the LASCO-C2 radial FoV. For both rotations, there is an overall good consistency between the AWSoM and the C2-SRT maps, both in terms of shape and size of the streamer belt and the CHs, as well as in terms of characteristic values and their dynamic range. The AWSoM model exhibits density values systematically somewhat larger than the tomographic results, as detailed below. The location and shape of the O/C boundaries of the AWSoM model reasonably match the transition of the C2-SRT N_e from larger values in the streamer belt (red/yellow colors) to smaller CHs values (green/blue colors).

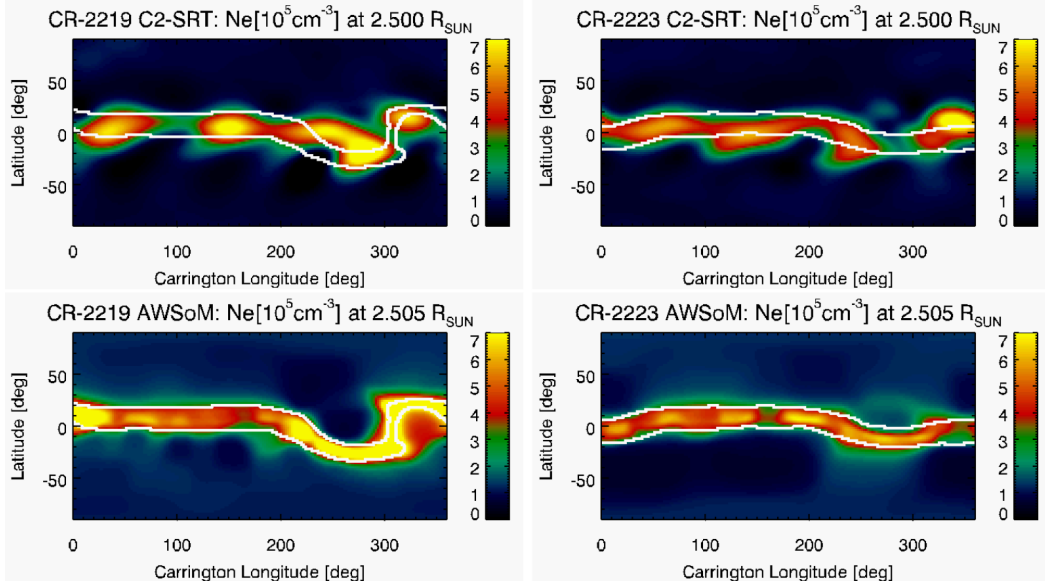


Figure 8. Latitude-longitude maps of electron density N_e for CR-2219 (left panels) and CR-2223 (right panels) at the heliocentric height $r = 2.5 R_\odot$, from LASCO-C2 tomography (C2-SRT, top panels) and from the AWSoM model (bottom panels). In each panel, the over plotted thick-white curves indicate the open/closed boundaries according to the AWSoM model.

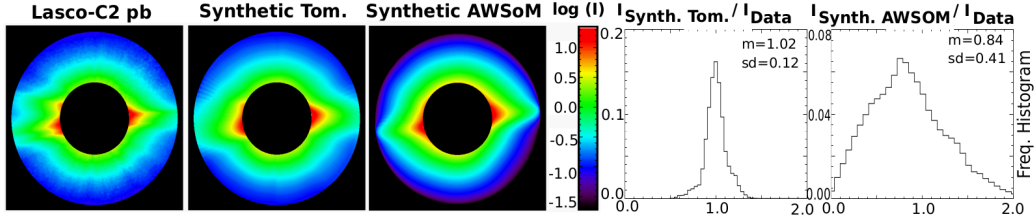


Figure 9. Comparison of an actual LASCO-C2 image (taken on 2019-10-16 UT 09) against synthetic ones. The images are masked (black color) outside the FoV radial range $2.5 - 6.0 R_\odot$. From left to right: LASCO-C2 pB -image, C2-SRT synthetic image, AWSoM synthetic image, and histograms of the pixel-by-pixel ratio $I_{\text{SYNTH}}/I_{\text{DATA}}$ for C2-SRT and AWSoM, respectively.

456 As in the previous section, comparison between synthetic images (derived from either
 457 C2-SRT or AWSoM) against actual data, constitutes a good validation test for both
 458 the reconstruction and the model. Figure 9 shows an example of a LASCO-C2 image as
 459 well as synthetic ones, and their comparison. C2-SRT images are again systematically
 460 more consistent with the actual LASCO-C2 images than the AWSoM synthetic images,
 461 as quantified by the comparative histograms. As an example of comparison of smaller-
 462 scale features among these images, note that in this specific case the East limb of the
 463 LASCO-C2 image, which corresponds to Carrington longitude $\approx 270^\circ$, shows a doubled
 464 peaked streamer. This feature is more faithfully reproduced by the C2-SRT synthetic
 465 image, while the AWSoM synthetic image shows only one peak.

466 For both rotations, C2-SRT and AWSoM results were traced along magnetic open
 467 field lines given by the MHD model, in the range of heights covered by the LASCO-C2

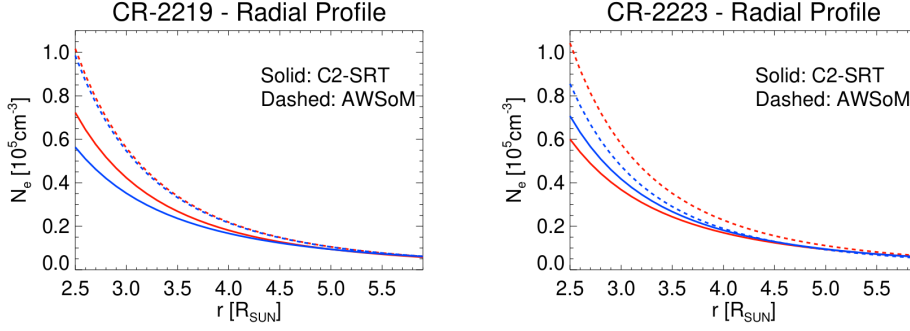


Figure 10. Average power law fits to $N_e(r)$ along open field lines traced in the northern CH (red) and the southern CH (blue) for CR-2219 (left panel) and CR-2223 (right panel). Solid lines correspond to C2-SRT results while dashed lines correspond to the AWSoM model.

468 FoV. To provide a summary of the 3D results for both rotations, Figure 10 shows the
 469 average power law fits to $N_e(r)$, as given by Eqn. (6), for the open field lines traced in
 470 the northern hemisphere (red color) and the southern one (blue color) separately. The
 471 C2-SRT results are plotted in solid line style and the AWSoM model results in dashed
 472 line style. For both rotations is evident that, compared to the tomographic results, the
 473 AWSoM model overestimates the electron density values in both hemispheres, as well
 474 as underestimates its scale height.

475 Figures 11 and 12 show the statistical distribution of results for CRs 2219 and 2223,
 476 respectively. Tomographic results are shown in solid line style and the AWSoM model
 477 results in dashed line style, with red curves indicating results for the northern hemisphere
 478 and blue curves corresponding to the southern hemisphere. Left panels show the elec-
 479 tron density at the lowest height of the LASCO-C2 FoV, i.e. $N_e(r = 2.5 R_\odot)$, while right
 480 panels show the height-averaged density scale height $\langle \lambda_N \rangle$ of the fit, as indicated by Eqn. (7).

481 Table 3 summarises a quantitative comparative analysis between the AWSoM model
 482 and the results of C2-SRT reconstructions. The uncertainty level of C2 pB values is es-
 483 timated to be $\approx 15\%$ (Frazin et al., 2012; Lamy et al., 2020). The uncertainty in the
 484 electron density introduced by the tomographic reconstruction is $\approx 10\%$, estimated from
 485 the spread of the $I_{\text{SYNTH}}/I_{\text{DATA}}$ histogram for C2-SRT shown in Fig. 9. Considering those
 486 estimates, the uncertainty of the electron density from the C2-SRT is $\Delta N_e \approx 20\%$, which
 487 implies for the scale height of the fitted power-law an uncertainty $\Delta \langle \lambda_N \rangle \approx 15\%$. In
 488 both rotations the electron density of the AWSoM model at height $2.5 R_\odot$ is $\approx 20\text{--}75\%$
 489 larger than that of the reconstruction (depending on the hemisphere and rotation), dif-
 490 ferences that are 2–3 times the uncertainty level of the C2-SRT electron density. The
 491 density scale height of the model is 10 – 20% smaller than that of the reconstruction,
 492 a difference that is comparable to the uncertainty of the C2-SRT scale height.

493 As a closing remark, from the median value of the histograms of the height-averaged
 494 scale height $\langle \lambda_N \rangle$, and Eqn. (7), the characteristic values of the exponent of the power
 495 law fits are ≈ 2.8 and ≈ 3.3 for the C2-SRT reconstructions and the AWSoM model,
 496 respectively. Finally, we also highlight that the characteristic values of λ_N from the C2-
 497 SRT analysis are far from consistent with a isothermal hydrostatic regime, for which $\lambda_N \approx$
 498 $1.5 R_\odot$ implies $T_e \approx 22$ MK, a clearly non-physical result in these coronal structures.
 499 It is expected that the solar wind electron density could not be approximated well by
 500 the hydrostatic regime approximation over the LASCO-C2 radial FoV, $2.5 - 6.0 R_\odot$,
 501 as anticipated in Sec. 2.3 in discussing the power law in Eqn. (6).

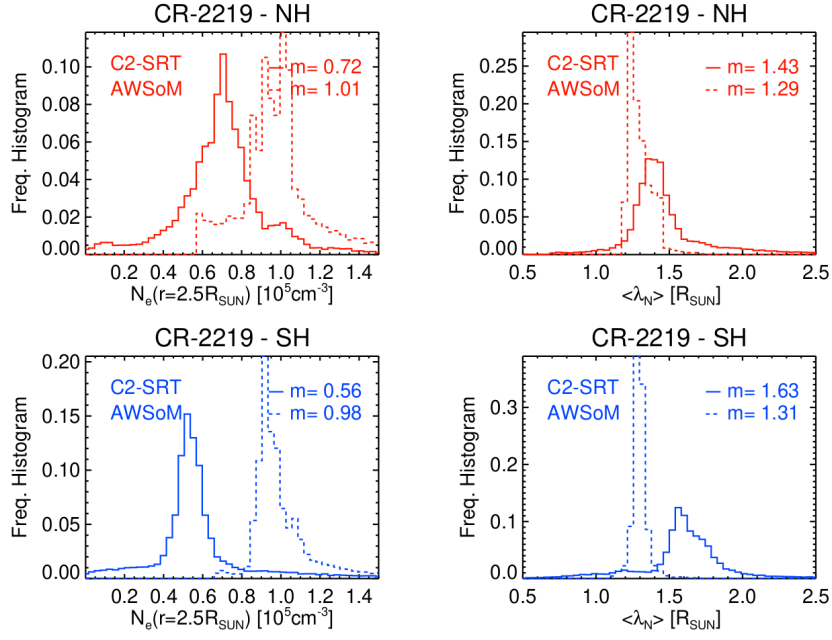


Figure 11. Statistical distribution of the results for CR-2219 from C2-SRT (solid lines) and AWSoM (dashed lines) traced along open field lines of the northern hemisphere (NH, top panels and red color) and the southern hemisphere (SH, bottom panels and blue color). The left panels show the electron density at the lowest heliocentric height of the LASCO-C2 FoV $N_e(r = 2.5R_{\odot})$, while the right panels show the electron density scale height $\langle \lambda_N \rangle$, height-averaged over the LASCO-C2 radial FoV. In each panel the median values m are indicated.

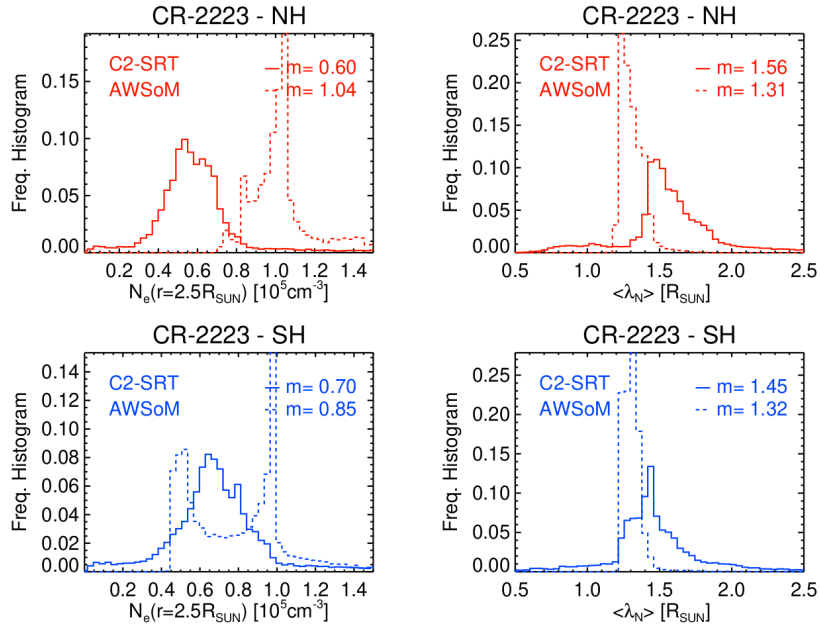


Figure 12. Same as Figure 11 for CR-2223.

Table 3. Median value (indicated as “Md”) of the statistical distribution of $N_e(r = 2.5 R_\odot)$ and $\langle \lambda_N \rangle$ shown in Figs. 11-12. C2-SRT values are expressed in absolute terms, while AWSoM results are expressed relative to the corresponding C2-SRT value.

Type	Md(N_e) [10^5 cm^{-3}]	Md($\langle \lambda_N \rangle$) [R_\odot]
CR-2219		
NH	0.72 (+40%)	1.43 (-10%)
SH	0.56 (+75%)	1.63 (-20%)
CR-2223		
NH	0.60 (+73%)	1.56 (-16%)
SH	0.70 (+21%)	1.45 (-9%)

502

3.3 Terminal Wind Speed and DEMA Results

503

504

505

506

507

508

509

510

511

512

513

514

The correlation between the terminal wind speed of the AWSoM model and the electron density and temperature of the low corona as derived from DEMA was investigated. Open field lines were traced from the coronal base up to a maximum height $r_M = 20 R_\odot$, where the model essentially reached its terminal properties. In order to evenly thread the volume of the open region, $N = 90 \times 180 = 16,200$ starting points were uniformly set in longitude and latitude (with a 2° spacing) at an intermediate heliocentric height of $r_0 = 6 R_\odot$, where closed field lines of the model are essentially absent. For each of the N starting points, the field line passing through that location was traced both inwards down to the coronal base as well as outwards up to r_M . For each traced field line, the DEMA field line averaged electron temperature $\langle T_e \rangle$ and the coronal base electron density $N_e(r = 1.05 R_\odot)$ were determined, as well as the AWSoM model terminal wind speed $V_r(r_M)$.

515

516

517

518

519

520

521

522

As shown by Figures 1, some open field lines of the model thread locations where the DEMA electron density is characteristic of the streamer belt region. As shown by the analysis of Figures 3, this discrepancy is most probably due to lack of accuracy of the ADAPT-GONG maps, and the DEMA electron density results at the coronal base can be used as a proxy to discern locations that belong to the streamer belt from those within the CHs. As in the previous sections, only field lines of type III were selected for analysis, as those are the ones which effectively thread CH regions according to the DEMA reconstructions.

523

524

525

526

527

528

529

530

531

532

533

The top panels of Figure 13 show latitude-longitude maps of the AWSoM model radial solar wind speed $V_r(r_M)$ for all selected open field lines, where the white regions correspond to non-selected field lines. For all field lines indicated in the top panels, middle panels show the scatter plots of the DEMA coronal base electron density $N_e(r = 1.05 R_\odot)$ versus the terminal radial wind speed $V_r(r_M)$ signed by B_r (i.e. multiplied by $\text{Sgn}(B_r)$) to separate results of the Northern and Southern hemispheres as positive and negative values, respectively. Similarly, the bottom panels show the scatter plots of the DEMA field line averaged electron temperature $\langle T_e \rangle$ versus $\text{Sg}(B_r) V_r(r_M)$. In middle and bottom panels the straight lines indicate the best Theil-Sen linear fit to the data in each hemisphere. The data points in the scatter plots are colored by the absolute value of the latitude of the field line at r_M .

534

535

536

These plots show that the model field lines threading the CHs exhibit a mean trend of anti-correlation between their terminal wind speed and both the DEMA electron density near the coronal base and the characteristic (field line averaged) DEMA electron tem-

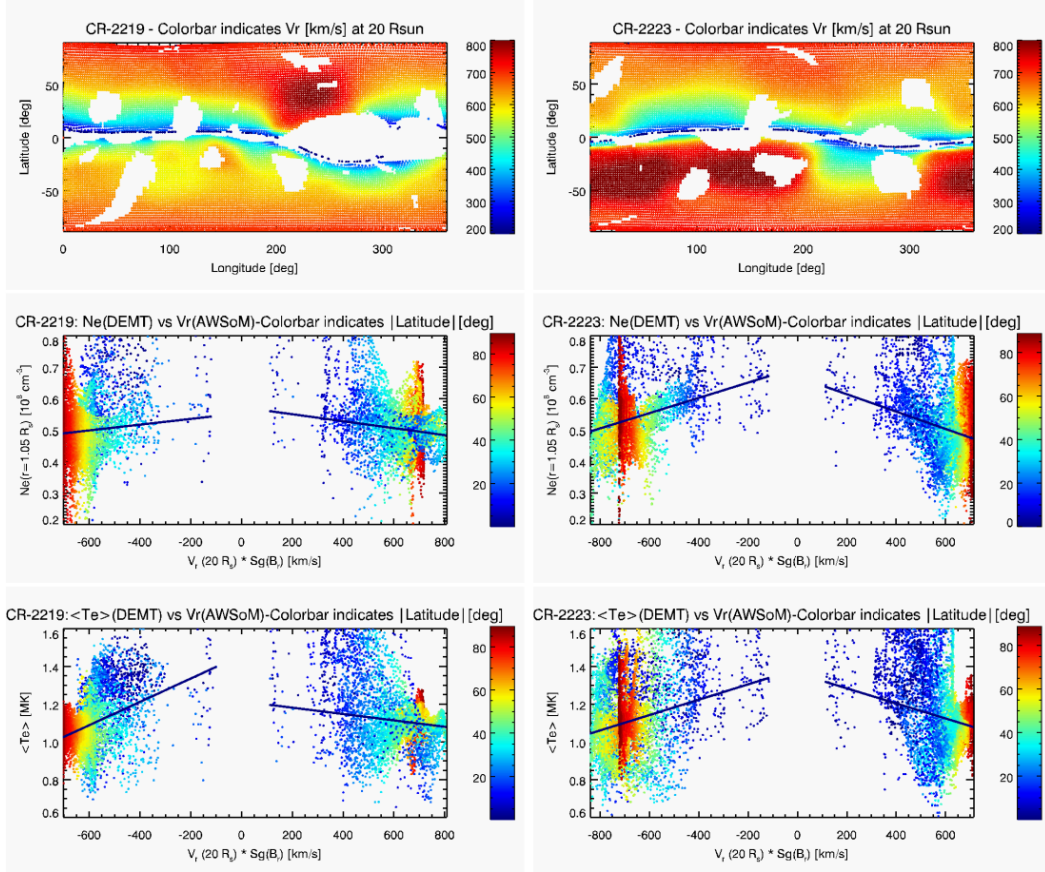


Figure 13. Top panels: latitude-longitude maps of the radial component of the AWSoM model terminal solar wind speed $V_r(r_M = 20 R_{\odot})$ [km s^{-1}], for CR-2219 (left panel) and CR-2223 (right panel), where each dot corresponds to a traced open field line that effectively threads a CH according to the DGMT reconstructions (see text in Section 3.3). Middle panels: scatter plots of the DGMT coronal base density $N_e(r = 1.05 R_{\odot})$ versus the AWSoM model terminal wind speed $V_r(r_M)$ signed by B_r (i.e. multiplied by $\text{Sgn}(B_r)$), for all field lines indicated in the top panels. Abscissa negative values correspond to the southern hemisphere and positive ones to the northern hemisphere. Bottom panels: scatter plots of the DGMT field line averaged electron temperature $\langle T_e \rangle$ versus $\text{Sg}(B_r) V_r(r_M)$, for the same field lines. In the middle and bottom panels, straight lines indicate the best Theil-Sen estimator linear fit to the data in each hemisphere. The colorbars indicate the module of the heliocentric latitude of the field line at heliocentric height r_M .

537 perature, for for both hemispheres of the two analysed rotations. The vertical spread of
 538 the data points around the observed trends (both for the density and temperature plots)
 539 is in the range $\approx 25 - 45\%$, depending on the rotation and hemisphere. This is con-
 540 sistent with the characteristic LDEM temperature spread W_T within each voxel, which
 541 as discussed in relation to Figure 2 is $\approx 45\%$ in CHs. Note also that slower terminal speeds
 542 tend to be found along field lines that terminate at lower latitudes, near the HCS, whose
 543 shape and location is bounded by the white contours in Figure 8. On the other hand,
 544 in general, the larger the terminal wind speed the larger the terminal latitude of the field
 545 line, except for localized regions (exhibiting the largest terminal speeds) in the North-
 546 ern hemisphere of CR-2219 and the Southern hemisphere of CR-2223.

4 Discussion and conclusions

The 3D thermodynamic structure of the global corona was studied for two WHPI campaign periods, CRs 2219 and 2223. Tomographic reconstructions of the electron density and temperature were carried out using EUV and WL images. Also, steady-state 3D MHD simulations of the two rotations were computed using the AWSoM model and compared in detail with the reconstructions.

The DENT reconstructions, which use AIA/SDO images, cover the range of heliocentric distance $1.02 - 1.25 R_{\odot}$, and their results are quantitatively summarized in Table 2. For both rotations, the DENT analysis shows that progressively outer layers of the equatorial streamer belt exhibit decreasing coronal base density, increasing density scale height, and increasing electron temperature. In transitioning from the closed region of the streamer out to the open regions of the CHs, the electron density at the coronal base and its scale height decrease, as well as the electron temperature. These trends are all in accordance with previous DENT studies (Lloveras et al., 2017, 2020) that analysed CRs 2081 and 2082, during the SC 23/24 deep minimum epoch. Compared to those rotations, the WHPI targets exhibit a $\approx 20\%$ lower coronal base density, a $\approx 20\%$ larger scale height and a $\approx 20\%$ larger electron temperature. Also, for both WHPI rotations the overall O/C structure of the AWSoM model agrees quite well with the density and temperature structure of DENT reconstructions, except between Carrington longitudes $\approx 0 - 200^{\circ}$ in the southern hemisphere, where the match is poorer. Comparison of synthetic images, computed from the DENT reconstructions and from the AWSoM model, against actual AIA data shows that those derived from tomography are significantly (and systematically) a better match, strongly suggesting that the adapt-GONG maps (here used as boundary conditions for AWSoM) are not accurate in the mismatch region. Quantitative comparison of the AWSoM model against the DENT reconstructions shows that the electron density at the coronal base agree with the tomographic results within their $\approx 10\%$ uncertainty. The scale height and electron temperature of the model are systematically $\approx 5 - 20\%$ smaller than the reconstructed values (depending on the rotation and coronal region), differences up to fourfold their $\lesssim 5\%$ uncertainty.

While quite successful matching the large-scale structure of the DENT reconstructions, the AWSoM model (used in its latest version for this study) does not reproduce small-scale coronal features systematically revealed by DENT. Firstly, loops with temperature decreasing with height (known as “down loops”) were found in the low latitudes within the streamer belt, as in previous DENT solar minima studies (Huang et al., 2012; Nuevo et al., 2013; Lloveras et al., 2017, 2020). Such structures are expected where heating is strongly enhanced at the coronal base. This has been explored by Schiff and Cranmer (2016), who used a 1D model to simulate down loops by including coronal heating dissipation of compressive waves formed by mode conversion from an initial population of Alfvén waves, a physical mechanism originally proposed by Nuevo et al. (2013). Secondly, as in previous DENT studies, the reconstructions reveal that the coronal plasma is ubiquitously characterized by a significant local temperature spread within the $\sim 10^4$ km linear size of the tomography computational cell (Vásquez, 2016). As shown in this study, the characteristic temperature spread of the LDEM (characterizing the temperature distribution of the plasma within an individual cell) is found to be $\approx 25\%$ in streamers and $\approx 45\%$ in CHs. Furthermore, streamers also exhibit multi-modal LDEM, resulting in even larger temperature dispersion within the tomographic cell’s spatial scale (Nuevo et al., 2015). Except across specific localized regions, such as the O/C boundaries, 3D-MHD models such as as AWSoM do not exhibit such fine structure (Shi et al., 2022). The LDEM is a measure of the temperature distribution across a large number of thermally isolated magnetic flux tubes threading any given individual tomographic cell. Its spread implies a similar degree of fine structure in the density within the cell, so that significant Alfvén speed gradients perpendicular to the field direction can be expected within that same spatial scale. We speculate that taking into account this level of fine-

600 structure by global 3D-MHD models may be significantly consequential for their predic-
601 tions on dynamics of phenomena in the solar corona, such as Alfvén wave propagation.

602 The WL-SRT reconstructions, which use SoHO/LASCO-C2 pB images, cover the
603 range of heliocentric distance 2.5–6.0 R_{\odot} , and their results are quantitatively summa-
604 rized in Table 3. For the two rotations analysed in this work, the reconstructed electron
605 density exhibits similar values and trends with height as those found in WL tomographic
606 reconstructions and global models of rotations selected from the SC 23/24 minimum epoch
607 (Vibert et al., 2016; T. Wang et al., 2017; Sachdeva et al., 2019; Morgan & Cook, 2020).
608 Quantitative comparison of the AWSoM model against the C2-SRT reconstructions shows
609 that the electron density of the model is 20–75% larger (depending on the hemisphere
610 and rotation) than the reconstructed values at the inner boundary of the LASCO-C2 ra-
611 dial FoV, a difference up to threefold their uncertainty. Also, within the C2 FoV, the
612 scale height of the electron density of the model is systematically 10–20% smaller than
613 the reconstructed values, a difference comparable to their $\approx 15\%$ uncertainty. Synthetic
614 images computed from C2-SRT reconstructions compare to actual LASCO-C2 data signifi-
615 cantly better than those computed from the AWSoM model, strongly suggesting that
616 the model overestimates the electron density in the FoV of LASCO-C2 by up to 75%.
617 This is likely due to the acceleration of the model being more gradual and extended (with
618 acceleration up to 15 R_{\odot} or more) than what is observed in large coronal holes. Future
619 planned enhancements of the AWSoM model include a multi-fluid description and im-
620 provement of the energy cascading process, which can both significantly affect the heat-
621 ing and acceleration of the solar wind model. In addition, we will include model valida-
622 tion from various observational data products including tomography.

623 We conclude discussing the results of the joint analysis of the DENT reconstruc-
624 tions and the solar wind velocity field of the AWSoM model. For both hemispheres of
625 the two analysed rotations, model’s field lines were traced threading the whole volume
626 of the CHs. It is found that the model’s terminal wind speed along field lines is anti-correlated
627 with their DENT reconstructed values of density and temperature at the low corona.
628 It is also found that the terminal latitude of the field lines tends to be larger for larger
629 terminal speeds, with the exception of specific localized regions of very high speed streams.
630 This analysis constitutes an interesting 3D validation of the AWSoM wind model, show-
631 ing that its slow component is associated with field lines that exhibit larger electron den-
632 sity and temperature near the streamer brightness boundary, forming the so called “streamer’s
633 legs” (Suess et al., 2009), that terminate near the HCS. On the other hand, the fast com-
634 ponent of the wind model is found to be associated with open field lines exhibiting rel-
635 atively lower values of DENT density and temperature, and terminating at larger lat-
636 itudes, deeper into the CHs. These results are consistent with the scenario in which, dur-
637 ing solar minima, the slow solar wind originates along open field lines closest to the streamer
638 belt while the fast wind originates from the CHs (Y. M. Wang & Sheeley, 1990).

639 This work is the third one of a series of tomographic studies aiming at character-
640 izing in 3D detail the global structure of the corona during the last three minima of solar
641 activity (Lloveras et al., 2017, 2020). In the context of the two specific WHPI peri-
642 ods chosen for study, this work also demonstrates the value of tomographic reconstruc-
643 tions for validation of 3D-MHD models. As new space borne and ground based solar tele-
644 scopes are coming into operation, further opportunities for development and application
645 of tomographic techniques will arise. Future projects will involve analysis of rotations
646 selected from epochs different than minima, over the current and previous SCs.

647 5 Open Research

648 Data Availability Statement:

649 The 3D tomographic reconstructions and 3D MHD simulations of the solar corona
650 and solar wind of WHPI targets CR-2219 and CR-2223 used in the article are available
651 at zenodo.org via DOI:10.5281/zenodo.6470700 (Lloveras et al., 2022).

652 Acknowledgments

653 The authors thank the reviews by the two anonymous referees, which provided construc-
654 tive insightful feedback that helped to improve and clarify this article. D.G. Lloveras ac-
655 knowledges CONICET fellowship (Res. Nro. 4870) that supported his participation in
656 this research. D.G. Lloveras, F.A. Nuevo, and A.M. Vásquez were partially supported
657 by ANPCyT grant PICT-2016/0221 to IAFE. The AIA/SDO data used in this study
658 is courtesy of NASA/SDO and the AIA, EVE, and HMI science teams.

659 References

- 660 Altschuler, M. D., & Perry, R. M. (1972, April). On Determining the Electron Den-
661 sity Distribution of the Solar Corona from K-Coronameter Data. *Solar Phys.*,
662 *23*(2), 410-428. doi: 10.1007/BF00148104
- 663 Arge, C. N., Henney, C. J., Hernandez, I. G., Toussaint, W. A., Koller, J., &
664 Godinez, H. C. (2013, June). Modeling the corona and solar wind us-
665 ing ADAPT maps that include far-side observations. , *1539*, 11-14. doi:
666 10.1063/1.4810977
- 667 Bisi, M. M., Thompson, B. J., Emery, B. A., Gibson, S. E., Leibacher, J., & van
668 Driel-Gesztelyi, L. (2011, December). The Sun-Earth Connection near
669 Solar Minimum: Placing it into Context. *Solar Phys.*, *274*(1-2), 1-3. doi:
670 10.1007/s11207-011-9915-2
- 671 Butala, M. D., Hewett, R. J., Frazin, R. A., & Kamalabadi, F. (2010, April). Dy-
672 namic Three-Dimensional Tomography of the Solar Corona. *Solar Phys.*, *262*,
673 495-509. doi: 10.1007/s11207-010-9536-1
- 674 Cairns, I. H., Lobzin, V. V., Warmuth, A., Li, B., Robinson, P. A., & Mann, G.
675 (2009, December). Direct Radio Probing and Interpretation of the Sun's
676 Plasma Density Profile. *Astrophys. J. Lett.*, *706*(2), L265-L269. doi:
677 10.1088/0004-637X/706/2/L265
- 678 Del Zanna, G., Dere, K. P., Young, P. R., Landi, E., & Mason, H. E. (2015, Oct).
679 CHIANTI - An atomic database for emission lines. Version 8. *Astron. Astro-*
680 *phys.*, *582*, A56. doi: 10.1051/0004-6361/201526827
- 681 Frazin, R. A., & Janzen, P. (2002, May). Tomography of the Solar Corona. II.
682 Robust, Regularized, Positive Estimation of the Three-dimensional Electron
683 Density Distribution from LASCO-C2 Polarized White-Light Images. *Astro-*
684 *phys. J.*, *570*, 408-422. doi: 10.1086/339572
- 685 Frazin, R. A., Vásquez, A. M., & Kamalabadi, F. (2009, August). Quantitative,
686 Three-dimensional Analysis of the Global Corona with Multi-spacecraft Dif-
687 ferential Emission Measure Tomography. *Astrophys. J.*, *701*, 547-560. doi:
688 10.1088/0004-637X/701/1/547
- 689 Frazin, R. A., Vásquez, A. M., Thompson, W. T., Hewett, R. J., Lamy, P., Llebaria,
690 A., . . . Burkepile, J. (2012, September). Intercomparison of the LASCO-C2,
691 SECCHI-COR1, SECCHI-COR2, and Mk4 Coronagraphs. *Solar Phys.*, *280*(1),
692 273-293. doi: 10.1007/s11207-012-0028-3
- 693 Galvin, A. B., & Kohl, J. L. (1999, May). Whole Sun Month at solar min-
694 imum: An introduction. *J. Geophys. Res.*, *104*(A5), 9673-9678. doi:
695 10.1029/1999JA900008
- 696 Guhathakurta, M., Holzer, T. E., & MacQueen, R. M. (1996, February). The Large-
697 Scale Density Structure of the Solar Corona and the Heliospheric Current
698 Sheet. *Astrophys. J.*, *458*, 817. doi: 10.1086/176860
- 699 Harding, J. C., Cairns, I. H., & Lobzin, V. V. (2019, May). Offset Power-law Depen-

- dence of the Sun's Radial Electron Density Profile: Evidence and Implications. *Astrophys. J.*, 877(1), 25. doi: 10.3847/1538-4357/ab19a0
- Huang, Z., Frazin, R. A., Landi, E., Manchester, W. B., Vásquez, A. M., & Gombosi, T. I. (2012, August). Newly Discovered Global Temperature Structures in the Quiet Sun at Solar Minimum. *Astrophys. J.*, 755, 86. doi: 10.1088/0004-637X/755/2/86
- Jin, M., Manchester, W. B., van der Holst, B., Oran, R., Sokolov, I., Toth, G., ... Sun, X. (2012, Dec). Simulate the Coronal Mass Ejection on 2011 March 7 from Chromosphere to 1 AU. In *Agu fall meeting abstracts* (Vol. 2012, p. SH33E-04).
- Kalman, R. E. (1960). A new approach to linear filtering and prediction problems. *Journal of Basic Engineering*, 82(1), 35. Retrieved from <http://dx.doi.org/10.1115/1.3662552> doi: 10.1115/1.3662552
- Kohl, J. L., Noci, G., Antonucci, E., Tondello, G., Huber, M. C. E., Cranmer, S. R., ... Suleiman, R. M. (1998, July). UVCS/SOHO Empirical Determinations of Anisotropic Velocity Distributions in the Solar Corona. *Astrophys. J. Lett.*, 501(1), L127-L131. doi: 10.1086/311434
- Lamy, P., Floyd, O., Mikić, Z., & Riley, P. (2019, November). Validation of MHD Model Predictions of the Corona with LASCO-C2 Polarized Brightness Images. *Solar Phys.*, 294(11), 162. doi: 10.1007/s11207-019-1549-9
- Lamy, P., Llebaria, A., Boclet, B., Gilardy, H., Burtin, M., & Floyd, O. (2020, July). Coronal Photopolarimetry with the LASCO-C2 Coronagraph over 24 Years [1996 - 2019]. *Solar Phys.*, 295(7), 89. doi: 10.1007/s11207-020-01650-y
- Lloveras, D. G., Vásquez, A. M., & Nuevo, F. A. (2022). *Data cubes corresponding to the article "three-dimensional structure of the corona during whp1 campaign rotations cr-2219 and cr-2223"* [dataset]. Retrieved from <https://doi.org/10.5281/zenodo.6470700> doi: 10.5281/zenodo.6470700
- Lloveras, D. G., Vásquez, A. M., Nuevo, F. A., & Frazin, R. A. (2017, October). Comparative Study of the Three-Dimensional Thermodynamical Structure of the Inner Corona of Solar Minimum Carrington Rotations 1915 and 2081. *Solar Phys.*, 292(10), 153. doi: 10.1007/s11207-017-1179-z
- Lloveras, D. G., Vásquez, A. M., Nuevo, F. A., Mac Cormack, C., Sachdeva, N., Manchester, W., ... Frazin, R. A. (2020, June). Thermodynamic Structure of the Solar Corona: Tomographic Reconstructions and MHD Modeling. *Solar Phys.*, 295(6), 76. doi: 10.1007/s11207-020-01641-z
- Lobzin, V. V., Cairns, I. H., & Robinson, P. A. (2008, April). Evidence for Wind-like Regions, Acceleration of Shocks in the Deep Corona, and Relevance of $1/f$ Dynamic Spectra to Coronal Type II Bursts. *Astrophys. J. Lett.*, 677(2), L129. doi: 10.1086/587980
- Morgan, H. (2019, May). An Atlas of Coronal Electron Density at $5R_{\odot}$. II. A Spherical Harmonic Method for Density Reconstruction. *Astrophys. J. Suppl.*, 242(1), 3. doi: 10.3847/1538-4365/ab125d
- Morgan, H., & Cook, A. C. (2020, April). The Width, Density, and Outflow of Solar Coronal Streamers. *Astrophys. J.*, 893(1), 57. doi: 10.3847/1538-4357/ab7e32
- Nuevo, F. A., Huang, Z., Frazin, R., Manchester, W. B., Jin, M., & Vásquez, A. M. (2013, Aug). Evolution of the Global Temperature Structure of the Solar Corona during the Minimum between Solar Cycles 23 and 24. *Astrophys. J.*, 773(1), 9. doi: 10.1088/0004-637X/773/1/9
- Nuevo, F. A., Vásquez, A. M., Landi, E., & Frazin, R. (2015, October). Multimodal Differential Emission Measure in the Solar Corona. *Astrophys. J.*, 811(2), 128. doi: 10.1088/0004-637X/811/2/128
- Ofman, L. (2010, October). Wave Modeling of the Solar Wind. *Living Reviews in Solar Physics*, 7(1), 4. doi: 10.12942/lrsp-2010-4
- Oran, R., Landi, E., van der Holst, B., Lepri, S. T., Vásquez, A. M., Nuevo, F. A.,

- 755 ... Gombosi, T. I. (2015, June). A Steady-state Picture of Solar Wind Ac-
 756 celeration and Charge State Composition Derived from a Global Wave-driven
 757 MHD Model. *Astrophys. J.*, *806*(1), 55. doi: 10.1088/0004-637X/806/1/55
- 758 Powell, K. G., Roe, P. L., Linde, T. J., Gombosi, T. I., & De Zeeuw, D. L. (1999,
 759 September). A Solution-Adaptive Upwind Scheme for Ideal Magnetohy-
 760 drodynamics. *Journal of Computational Physics*, *154*(2), 284-309. doi:
 761 10.1006/jcph.1999.6299
- 762 Sachdeva, N., Tóth, G., Manchester, W. B., van der Holst, B., Huang, Z., Sokolov,
 763 I. V., ... Vásquez, A. M. (2021, December). Simulating Solar Maximum
 764 Conditions Using the Alfvén Wave Solar Atmosphere Model (AWSoM). *As-
 765 trophys. J.*, *923*(2), 176. doi: 10.3847/1538-4357/ac307c
- 766 Sachdeva, N., van der Holst, B., Manchester, W. B., Tóth, G., Chen, Y., Lloveras,
 767 D. G., ... Henney, C. J. (2019, December). Validation of the Alfvén Wave
 768 Solar Atmosphere Model (AWSoM) with Observations from the Low Corona to
 769 1 au. *Astrophys. J.*, *887*(1), 83. doi: 10.3847/1538-4357/ab4f5e
- 770 Schiff, A. J., & Cranmer, S. R. (2016, Nov). Explaining Inverted-temperature Loops
 771 in the Quiet Solar Corona with Magnetohydrodynamic Wave-mode Conver-
 772 sion. *Astrophys. J.*, *831*(1), 10. doi: 10.3847/0004-637X/831/1/10
- 773 Shi, T., Manchester, I., Ward, Landi, E., van der Holst, B., Szenté, J., Chen, Y., ...
 774 Pevtsov, A. (2022, March). AWSoM Magnetohydrodynamic Simulation of a
 775 Solar Active Region with Realistic Spectral Synthesis. *Astrophys. J.*, *928*(1),
 776 34. doi: 10.3847/1538-4357/ac52ab
- 777 Sittler, J., Edward C., & Guhathakurta, M. (1999, October). Semiempirical Two-
 778 dimensional MagnetoHydrodynamic Model of the Solar Corona and Interplane-
 779 tary Medium. *Astrophys. J.*, *523*(2), 812-826. doi: 10.1086/307742
- 780 Sokolov, I. V., van der Holst, B., Oran, R., Downs, C., Roussev, I. I., Jin, M., ...
 781 Gombosi, T. I. (2013, February). Magnetohydrodynamic Waves and Coronal
 782 Heating: Unifying Empirical and MHD Turbulence Models. *Astrophys. J.*,
 783 *764*(1), 23. doi: 10.1088/0004-637X/764/1/23
- 784 Suess, S. T., Ko, Y. K., von Steiger, R., & Moore, R. L. (2009, April). Quiescent
 785 current sheets in the solar wind and origins of slow wind. *Journal of Geophysi-
 786 cal Research (Space Physics)*, *114*(A4), A04103. doi: 10.1029/2008JA013704
- 787 Thernisien, A. F., & Howard, R. A. (2006, May). Electron Density Modeling of
 788 a Streamer Using LASCO Data of 2004 January and February. *Astrophys. J.*,
 789 *642*(1), 523-532. doi: 10.1086/500818
- 790 Tóth, G., van der Holst, B., Sokolov, I. V., De Zeeuw, D. L., Gombosi, T. I., Fang,
 791 F., ... Opher, M. (2012, Feb). Adaptive numerical algorithms in space
 792 weather modeling. *Journal of Computational Physics*, *231*(3), 870-903. doi:
 793 10.1016/j.jcp.2011.02.006
- 794 van der Holst, B., Manchester, I., W. B., Frazin, R. A., Vásquez, A. M., Tóth,
 795 G., & Gombosi, T. I. (2010, Dec). A Data-driven, Two-temperature Solar
 796 Wind Model with Alfvén Waves. *Astrophys. J.*, *725*(1), 1373-1383. doi:
 797 10.1088/0004-637X/725/1/1373
- 798 van der Holst, B., Sokolov, I. V., Meng, X., Jin, M., Manchester, I., W. B., Tóth, G.,
 799 & Gombosi, T. I. (2014, Feb). Alfvén Wave Solar Model (AWSoM): Coronal
 800 Heating. *Astrophys. J.*, *782*(2), 81. doi: 10.1088/0004-637X/782/2/81
- 801 Van Doorselaere, T., Srivastava, A. K., Antolin, P., Magyar, N., Vasheghani Fara-
 802 hani, S., Tian, H., ... Pascoe, D. (2020, December). Coronal Heating by MHD
 803 Waves. *Space Sci. Rev.*, *216*(8), 140. doi: 10.1007/s11214-020-00770-y
- 804 Vásquez, A. M. (2016, March). Seeing the solar corona in three dimensions. *Ad-
 805 vances in Space Research*, *57*, 1286-1293. doi: 10.1016/j.asr.2015.05.047
- 806 Vásquez, A. M., Frazin, R. A., & Kamalabadi, F. (2009, May). 3D Tempera-
 807 tures and Densities of the Solar Corona via Multi-Spacecraft EUV Tomog-
 808 raphy: Analysis of Prominence Cavities. *Solar Phys.*, *256*(1-2), 73-85. doi:
 809 10.1007/s11207-009-9321-1

- 810 Vázquez, A. M., Frazin, R. A., & Manchester, I., Ward B. (2010, June). The So-
811 lar Minimum Corona from Differential Emission Measure Tomography. *Astro-*
812 *phys. J.*, 715(2), 1352-1365. doi: 10.1088/0004-637X/715/2/1352
- 813 Vázquez, A. M., Huang, Z., Manchester, W. B., & Frazin, R. A. (2011, December).
814 The WHI Corona from Differential Emission Measure Tomography. *Solar*
815 *Phys.*, 274(1-2), 259-284. doi: 10.1007/s11207-010-9706-1
- 816 Vibert, D., Peillon, C., Lamy, P., Frazin, R. A., & Wojak, J. (2016, October). Time-
817 dependent tomographic reconstruction of the solar corona. *Astronomy and*
818 *Computing*, 17, 144-162. doi: 10.1016/j.ascom.2016.09.001
- 819 Wang, T., Reginald, N. L., Davila, J. M., St. Cyr, O. C., & Thompson, W. T.
820 (2017, August). Variation in Coronal Activity from Solar Cycle 24 Mini-
821 mum to Maximum Using Three-Dimensional Reconstructions of the Coro-
822 nal Electron Density from STEREO/COR1. *Solar Phys.*, 292(8), 97. doi:
823 10.1007/s11207-017-1130-3
- 824 Wang, Y. M., & Sheeley, J., N. R. (1990, June). Solar Wind Speed and Coronal
825 Flux-Tube Expansion. *Astrophys. J.*, 355, 726. doi: 10.1086/168805